Volume 10 | Number 39 | 21 October 2018 | Pages 18427–18894

Nanoscale

rsc.li/nanoscale

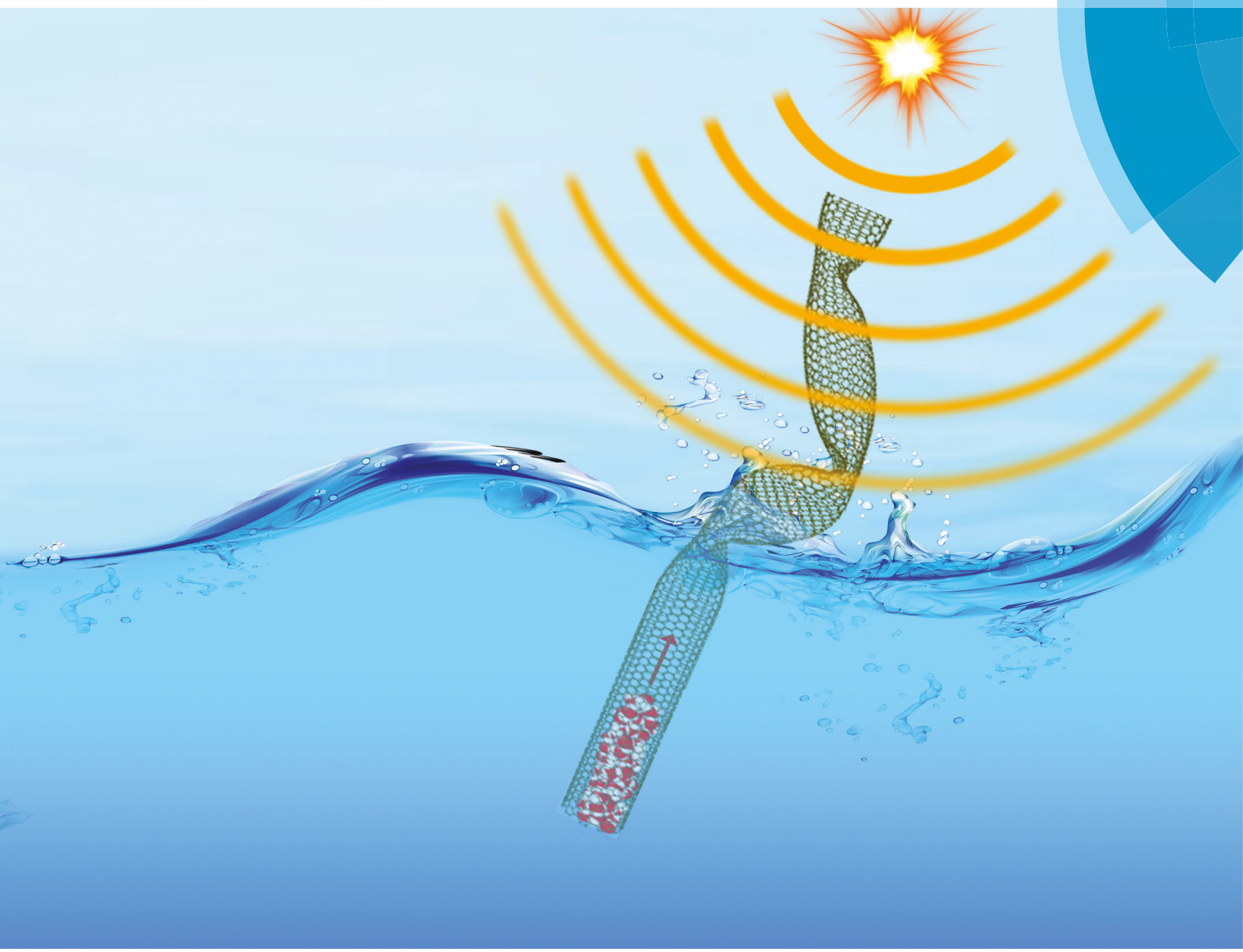

ISSN 2040-3372

ROYAL SOCIETY OF CHEMISTRY

COMMUNICATION
Baoxing Xu, Weiyi Lu *et al.*
Compressing liquid nanofoam systems: liquid infiltration or nanopore deformation?

NCNST

Nanoscale

COMMUNICATION

View Article Online
View Journal | View Issue

Cite this: *Nanoscale*, 2018, **10**, 18444

Received 24th May 2018,
Accepted 30th July 2018

DOI: 10.1039/c8nr04233k

rsc.li/nanoscale

Compressing liquid nanofoam systems: liquid infiltration or nanopore deformation?†

Yue Zhang,‡[a] Mingzhe Li, ‡[b] Yuan Gao,[a] Baoxing Xu *[a] and Weiyi Lu *[b]

Understanding the invasion of a liquid into porous structures is the foundation of the characterization of the porosity-related properties of materials and is also of fundamental importance in the design of porous solid–liquid enabled energy protection systems, yet whether solid pores deform has been unclear so far. Here, we present a competition mechanism between liquid infiltration and cell wall buckling deformation by investigating a liquid nanofoam (LN) system subjected to quasi-static compression. The critical buckling stress of the cell wall and the infiltration pressure of liquid invasion into nanopores are studied and correlated through numerical simulation and experimental validation to reveal the quantitative relationship between nanopore deformation and liquid invasion. The analysis shows that liquid infiltration occurs, independent of the axial buckling stress of the cell wall; in contrast, the nanopore collapses radially when the radial collapse pressure is lower than the pressure of liquid infiltration, preventing the liquid invasion. Comprehensive molecular dynamics (MD) simulations are performed and demonstrate the deformation behavior of nanopores and cell wall–liquid interactions in a broad range. Pressure-induced compression experiments on a silica-based LN system are carried out and validate these theoretical and MD results.

Liquid intrusion porosimetry techniques such as mercury porosimetry have been widely used in the measurement of pore size distributions and pore volumes in both chemical and materials science engineering.[1] In particular, when porous structures are non-wettable to a liquid, an external pressure is applied to overcome the capillary force, which leads to the subsequent transport of the liquid into the pores. During this process, the associated mechanical energy will be partially converted into solid–liquid interactions and partially dissipated due to friction. Inspired by this unique phenomenon, a liquid nanofoam system has been developed to design energy protection layers and structures.[2–5] When the pore size is down to the nanoscale, the associated energy dissipation can be as high as 100 J g^{-1} due to the ultra-large surface area of nanopores (~100–1000 m^2 g^{-1}), several orders of magnitude higher than that of conventional energy absorption materials.[6,7] Besides, upon unloading, the liquid molecules flow out of the nanopores due to the hydrophobic nature of the porous surfaces, making the system fully reusable.[8] In both the measurement of pore distribution and design of energy dissipation structures, the underlying mechanism is the infiltration and transport of liquid molecules to pore spaces under a quasi-static pressure.[9–11] For hydrophobic nanopores, however, whether the liquid infiltration or buckling/collapse of empty nanopores occurs upon compression is fundamentally unanswered. The elucidation of this deformation competition mechanism will offer immediate guidance for designing high-performance liquid–solid porous energy protective structures and for estimating porosity-related characteristics of materials *via* porosimetry. In addition, the understanding of this competition mechanism could provide important insights into the stability assessment of other systems composed of fluid and nanoporous materials such as water transportation[12] and drug delivery systems.[13]

Here, we have investigated hydrophobic cylindrical nanopores, *i.e.* nanotubes, suspended in a liquid environment system subjected to a quasi-static loading, and generated a quantitative model to reveal the competition mechanism between liquid infiltration and nanopore buckling/collapse. Two different deformation models of the nanopore, axial buckling and radial collapse, are identified and incorporated with liquid infiltration. The theoretical analysis shows that liquid infiltration only depends on the critical pressure of radial collapse. When the liquid infiltration pressure is lower than the critical radial collapse pressure, the liquid invades into nanopores. Otherwise, the nanopore buckles and collapses along the radial direction, and thus, the liquid cannot be infiltrated

[a]*Department of Mechanical and Aerospace Engineering, University of Virginia, Charlottesville, VA 22904, USA. E-mail: bx4c@virginia.edu*
[b]*Department of Civil and Environmental Engineering, Michigan State University, East Lansing, MI 48824, USA. E-mail: wylu@egr.msu.edu*

†Electronic supplementary information (ESI) available. See DOI: 10.1039/c8nr04233k

‡These authors contributed equally to this work.

into the nanopores. By contrast, liquid infiltration always happens, independent of the axial buckling stress of the nanopore. Extensive molecular dynamics (MD) simulations have been performed on a liquid–nanotube system under a quasi-static pressure. Both the surface wettability and size dimension of the nanopore are considered, and the simulation results show good agreement with the theoretical analysis. Furthermore, compression experiments on a silica-based LN system have been conducted which confirmed the findings.

Fig. 1(a) illustrates a non-wetting flexible nanotube immersed in a liquid environment, and the nanotube is empty due to the nature of the hydrophobic nanopore surface. Upon applying a pressure, the nanotube is subjected to a uniform compression, leading to either infiltration of the liquid into the nanotube or deformation of the nanotube. Based on the Laplace–Young equation, the critical pressure for liquid infiltration can be determined quantitatively *via* $P_{\text{in}} = \dfrac{-4\gamma[\cos\theta]}{D}$, where γ is the surface tension between water and air/vacuum, θ is the contact angle between the nanotube surface wall and water molecules and represents the surface wettability of the nanotube, and D is the diameter of the nanotube. For example, taking water as the liquid and a silica nanotube (SNT) as the pore, which can be easily achieved and verified in experiments, respectively, the surface tension γ = 100.75 MPa nm can be obtained from a series of molecular dynamics simulations on the pressure-induced infiltration of water molecules into SNTs with diameter D = 1.4 nm (Fig. S1 and 2 in the ESI†). We should note that when the size dimension and materials of the tubes change, γ can also be determined by following similar procedures. In addition to the possible mechanism of liquid infiltration, given the large aspect ratio of SNT pores, axial buckling or radial collapse might happen, leading to pore deformation. Assume that the mechanical deformation energy of the nanotube is $E = \lambda E_0$, where λ is the energy coefficient and reflects the deformation ability of SNTs, and E_0 is the deformation energy of a pristine SNT. According to the buckling theory, the critical pressure of axial buckling $P^{\text{cr}}_{\text{axial}}$ for the flexible nanotube is determined quantitatively *via* $P^{\text{cr}}_{\text{axial}} = \dfrac{C_1\lambda(D^2+h^2)}{L^2}$,[14,15] where L is the length of the nanotube, h is the thickness of the nanotube wall, and $C_1\lambda$ is an elastic constant of relevance to the axial compressive stiffness of the nanotubes. Similarly, the radial critical collapse pressure $P^{\text{cr}}_{\text{radial}}$ is determined quantitatively *via* $P^{\text{cr}}_{\text{radial}} = \dfrac{C_2\lambda}{D^3}$,[16,17] and is independent of the length of the nanotube, where $C_2\lambda$ is an elastic constant and depends on the radial stiffness of the nanotubes. For example, considering a pristine silica nanotube (SNT) with a diameter D = 1.4 nm and λ = 1, the simulations on the uniaxial and hydrostatic compression of SNTs show that C_1 = 159.16 GPa and C_2 = 1.93 GPa nm^3 (Fig. S3–5 in the ESI†).

Based on the above theoretical analysis, the quantitative relationship between P_{in}, $P^{\text{cr}}_{\text{axial}}$and $P^{\text{cr}}_{\text{radial}}$ can be calculated and apparently it depends on the geometry and surface wettability of the nanotube. The transition between axial buckling and liquid infiltration can be determined *via* $P_{\text{in}} = P^{\text{cr}}_{\text{axial}}$, and it is $\cos\theta = -\dfrac{C_1\lambda(D^3+Dh^2)}{4\gamma L^2}$. Similarly, $\cos\theta = -\dfrac{C_2\lambda}{4\gamma D^2}$ *via* $P_{\text{in}} = P^{\text{cr}}_{\text{radial}}$ which corresponds to the transition between radial collapse and liquid infiltration. As an example, taking λ = 0.3 and D = 1.4 nm and assuming a series of L and θ, Fig. 1(b) presents a theoretical map of the critical pressure for pore mechanical deformation and liquid infiltration. Generally, a liquid is expected to invade into the nanopore when P_{in} is smaller than $P^{\text{cr}}_{\text{radial}}$; otherwise, the pore is expected to collapse along the radial direction, and as a consequence, the liquid cannot be infiltrated into the nanopores. By contrast, the presence of an incompressible liquid medium surrounding the nanotube provides a strong lateral constraint to the nanotube and suppresses the axial buckling of the nanopores. Consequently, the

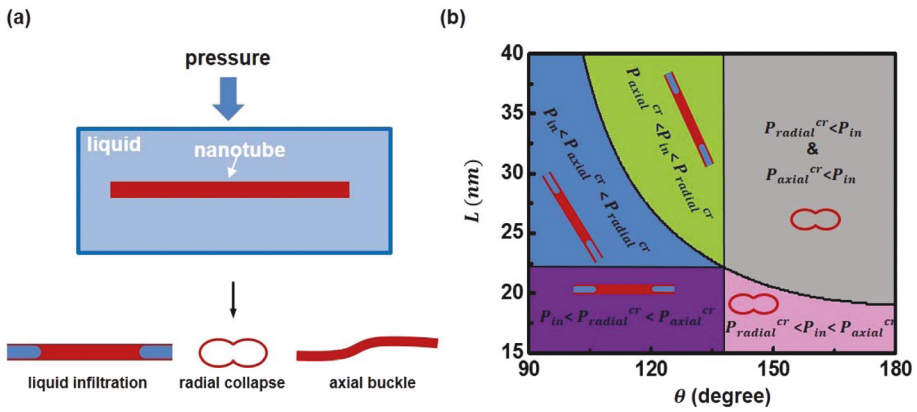

Fig. 1 Theoretical analysis of liquid infiltration and nanopore deformation for a liquid nanofoam system subjected to a quasi-static pressure. (a) Schematics of the non-wetting liquid–nanotube composite system under compression, and three deformation mechanisms: liquid infiltration, radial collapse and axial buckling of the nanopore. (b) Quantitative relationship among the critical pressure for liquid infiltration P_{in}, axial buckle $P^{\text{cr}}_{\text{axial}}$ and radial collapse $P^{\text{cr}}_{\text{radial}}$, with the variation of surface wettability represented by the contact angle θ and the tube length L. The tube diameter D = 1.4 nm and the deformation energy factor λ = 0.3.

liquid infiltration dominates the deformation process, independent of P^{cr}_{axial} which will be elucidated below in both molecular dynamics simulations and experiments. When D or λ changes, similar phase diagrams can be obtained, as shown in Fig. S6(a)–(c).† In particular, for a large λ, the nanotube will be very stiff, both P^{cr}_{axial} and P^{cr}_{radial} are far greater than P_{in}, and only liquid infiltration will happen, independent of the contact angle; for a small λ, the nanotube will become very soft, and the system may be mainly dominated by the radial collapse of the nanotube.

Molecular dynamics (MD) simulations were first performed to validate the competition of liquid infiltration and cell wall buckling. Fig. 2(a) shows the MD simulation model. Water was employed as the liquid phase and a silica nanotube (SNT) was adopted to model a nanopore. An SNT with length L and diameter D was immersed in a water reservoir. The initial density of water inside the reservoir was the same as that of bulk water, ρ_0 = 998.0 kg m^{-3}. The left and right boundaries of the reservoir were bound by two rigid walls, with the right one fixed and the left one movable to mimic a piston. Periodic boundary conditions were imposed on the other four lateral planes of the computational cell. An extended simple point charge (SPC/E) model was used to model water molecules[18] and the Tersoff potential was utilized to model the flexible SNT.[19] The 12-6 Lennard-Jones (L-J) potential and a Coulomb potential were used to describe the intermolecular potential between atoms.[20]

In the equilibration state, the water molecules stayed outside the SNT due to its hydrophobic nature. After this, the piston started to move to apply a quasi-static pressure to the system. All simulations were performed in the NVT ensemble with a Nose/Hoover thermostat[21] at a temperature of 300 K. The simulations were performed using the LAMMPS package.[22] More details of the MD simulation are given in the ESI.† In the simulations, to mimic the effect of the surface wettability of SNTs which can be achieved through surface treatments such as the decoration of functional groups on silicon atoms,[20] the interactive well depth between the silicon

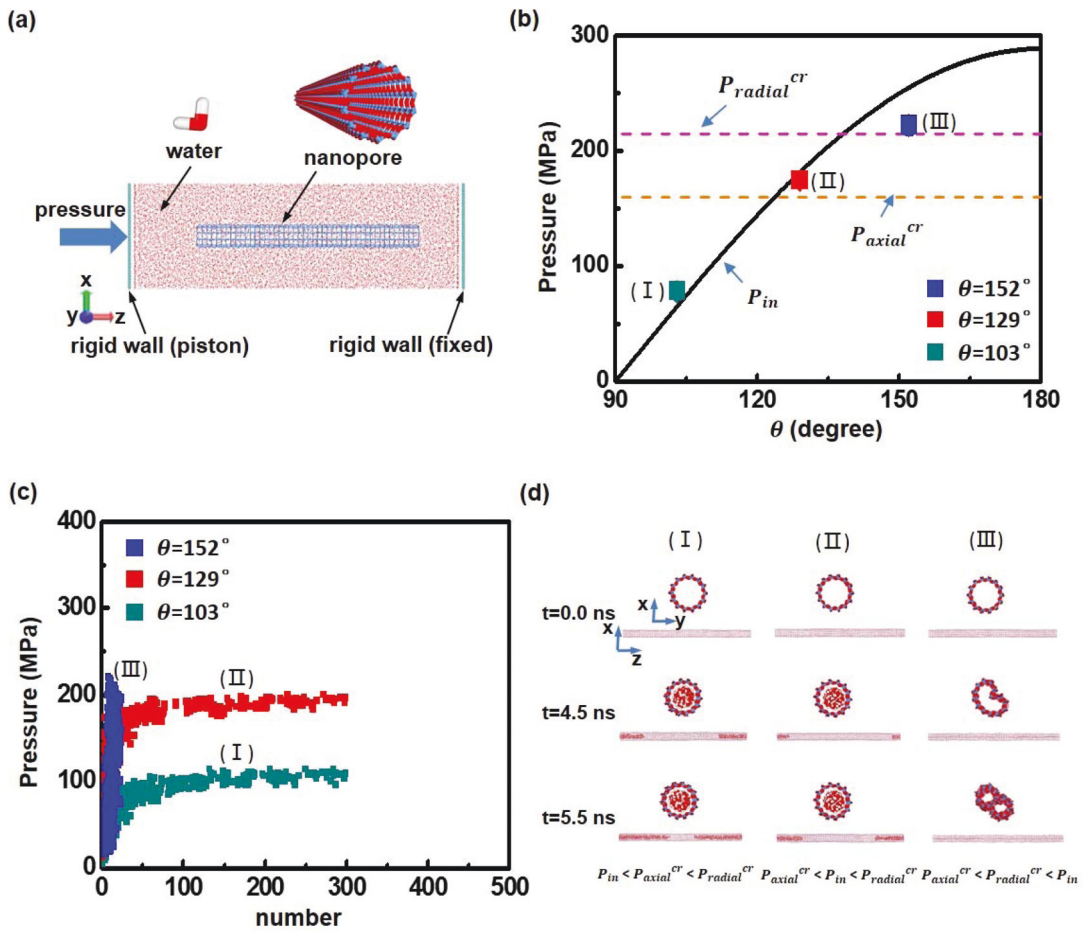

Fig. 2 Molecular dynamics simulations of pressure-induced liquid infiltration into a long nanopore. (a) Computational model of the water–nanopore system under compression (white: hydrogen atoms; red: oxygen atoms; blue: silicon atoms). (b) Critical axial buckle pressure and radial collapse pressure of the nanopore and the variation of critical infiltration pressure with different surface wettabilities (characterized *via* θ). (c) Variation of the number of infiltrated water molecules into the nanotube with different surface wettabilities. (d) Snapshots of the MD simulation at different simulation times (bottom: side view; top: axial view). The pore dimensions: D = 1.4 nm and L = 25 nm and the deformation energy factor: λ = 0.3.

atoms in SNTs and oxygen atoms in water molecules in the L-J potential, ε_{si-o}, was adjusted, as shown in Fig. S1;† the mechanical stiffness of the SNT was tuned by adjusting the deformation energy *via* λ to achieve all the possible quantitative conditions among P_{in}, P^{cr}_{axial} and P^{cr}_{radial}. For example, taking the geometry and strain energy tuning factor of the SNT D = 1.4 nm, L = 25 nm and λ = 0.3, the critical pressure for axial buckling P^{cr}_{axial} and radial collapse P^{cr}_{radial} of the SNT can be determined, and when the contact angle θ increases from 90° to 180°, the infiltration pressure P_{in} increases, as shown in Fig. 2(b). As a consequence, we can have three categories as $P_{in} < P^{cr}_{axial} < P^{cr}_{radial}$ at θ < 124°, $P^{cr}_{axial} < P_{in} < P^{cr}_{radial}$ at 124° < θ < 139°, and at θ > 139°, where P_{in} becomes larger than both P^{cr}_{axial} and P^{cr}_{radial}.

Considering three cases with the contact angle θ = 103°, θ = 129° and θ = 152°, Fig. 2(c) shows the variation of the number of infiltrated water molecules with the applied pressure *via* the piston. At θ = 103°, based on the above theoretical analysis, P_{in} = 70 MPa, and $P_{in} < P^{cr}_{axial}$ = 160 MPa < P^{cr}_{radial} = 215 MPa. When the applied pressure is relatively low, only a few water molecules are oscillated near the entrance of the SNT. When the pressure is beyond the critical value of P_{in} = 77 MPa, the capillary resistance is overcome and water molecules burst into the SNT with an arrival of a subsequent plateau stage of pressure. At θ = 129, P_{in} = 182 MPa, and $P^{cr}_{axial} < P_{in} < P^{cr}_{radial}$, the water molecules can still flow into the SNT, similar to that at θ = 103°, but with a larger infiltration pressure P_{in} = 175 MPa due to the higher hydrophobicity of the SNT. In contrast, when the contact angle θ = 152°, where P_{in} = 255 MPa is larger than both P^{cr}_{axial} = 160 MPa and P^{cr}_{radial} = 215 MPa, the nanotube is radially collapsed when the applied pressure comes to ~220 MPa, smaller than P_{in}. No water molecules are able to infiltrate into the SNT. Fig. 2(d) shows the corresponding snapshots of the SNTs and invaded water molecules at different simulation times. Clearly, for θ = 103°, water molecules are observed in the SNT at t = 4.5 ns and they increase with the simulation time. At the same time, the SNT morphology maintains the initial straight shape during the entire simulation, indicating no axial buckling or radial collapse. Similarly, in the case of θ = 129°, water molecules infiltrate into the SNT but with a smaller number due to a higher P_{in} at the same simulation time. More importantly, the SNT morphology remains straight, indicating that the axial buckling of the SNT does not take place even with $P^{cr}_{axial} < P_{in}$. When the contact angle θ increases to 152°, the SNT collapses radially at t = 4.5 ns and is further compressed with the increase of simulation time. As a consequence, no water molecule is observed in the SNT, indicating that the radial collapse of the solid nanopore dominates the deformation progress in a liquid–nanopore system with $P_{in} > P^{cr}_{radial}$. Fig. S7† shows the variation of the applied pressure with simulation time, and a sudden drop further confirms the radial collapse. These simulation results verify the theoretical assumption that the presence of a liquid environment suppresses the axial buckling of nanopores and consequently, the liquid infiltration dominates the deformation process, no matter P^{cr}_{axial} is greater or smaller than P_{in}.

To further validate the competition between liquid infiltration and solid nanotube buckling, we considered a short SNT with L = 20 nm, and accordingly the axial buckle pressure P^{cr}_{axial} increases to 260 MPa while P^{cr}_{radial} = 215 MPa does not change, leading to $P^{cr}_{axial} > P^{cr}_{radial}$. Following similar simulation procedures, further MD simulations were performed. Fig. 3(a) shows that the water molecules can infiltrate into the SNT at θ = 129°, where P_{in} is smaller than both P^{cr}_{axial} and P^{cr}_{radial}. When the contact angle θ increases to 152°, where P_{in} is greater than P^{cr}_{radial} but smaller than P^{cr}_{axial}, the SNT collapses in the radial direction when the applied pressure exceeds P^{cr}_{radial} = 220 MPa, yet is smaller than P_{in}. There is no infiltration of water molecules into the SNT. Fig. 3(b) shows the corresponding simulation snapshots of SNTs and infiltrated water molecules. Similar to the observations in Fig. 2(d), no axial buckling or radial collapse of the SNT is observed when $P_{in} < P^{cr}_{radial}$, and water molecules successfully invade into the SNTs; while the radial collapse of the nanopore occurs once $P^{cr}_{radial} < P_{in}$. Fig. S8† shows the density profile of water inside the SNTs along the radial direction of the SNT with different SNT lengths and wettabilities after the water molecules have intruded into the nanopore. The fluctuation of these density profiles represents the liquid–solid interaction in the confined nanotube and becomes larger for a smaller contact angle.[23]

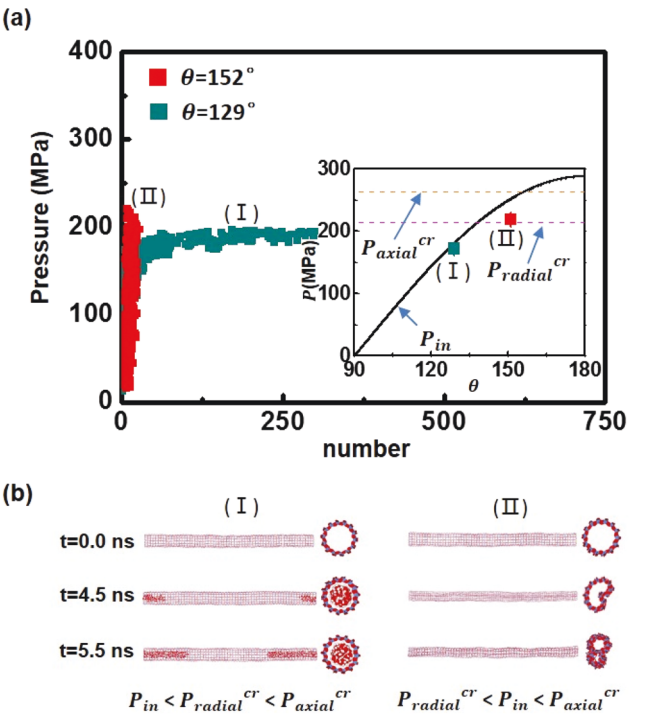

Fig. 3 Molecular dynamics simulations of pressure-induced liquid infiltration into a short nanopore. (a) Variation of the number of infiltrated water molecules into the nanotube with different surface wettabilities. The inset shows that the critical axial buckle pressure is larger than the radial collapse pressure of the SNT. (b) Snapshots of the MD simulation at different simulation times (left: side view; right: axial view). The pore dimension: D = 1.4 nm and L = 20 nm and the deformation energy factor: λ = 0.3.

However, given the same contact angle, the same configuration of the confined water molecules is obtained once water molecules are invaded into the SNT, and are independent of P^{cr}_{axial}, further confirming that there is no mechanical deformation of the SNTs even at $P^{cr}_{axial} < P_{in}$ when the length of the SNT increases from 20 nm to 25 nm. These simulation results further verify the theoretical assumption that when P_{in} is smaller than P^{cr}_{radial}, the liquid is expected to invade into the nanopore; when P_{in} becomes greater than P^{cr}_{radial}, the pore is expected to collapse along the radial direction.

To qualitatively validate the theoretical model and simulation results, we further performed quasi-static compression experiments on a silica-based LN system. The nanoporous silica particles (Perform-O-Sil 668, Nottingham Corp.) were hydrophobic and the average pore diameter was 115 nm. This LN consisting of 0.2 g of nanoporous silica and 2 g of saturated lithium chloride (LiCl) aqueous solution (46 wt%) was sealed in a stainless-steel cylinder using two pistons with O-rings and compressed by using a universal tester (Model 5982, Instron, Inc.) at a constant rate of 1 mm min^{-1}, as illustrated in Fig. 4(a). Once the desired peak force was reached, the crosshead of the Instron was moved back at the same velocity. The specific volume change of the LN samples was defined as $\Delta V = A\delta/m$, where A is the cross-sectional area of the pistons of 126 mm^2, δ is the displacement of the piston, and m is the mass of silica gel.

The same experimental setup was adopted for dry pre-compression on nanoporous silica particles without the presence of a liquid. Different peak forces applied on three silica gel samples were 0.25 kN, 0.50 kN and 0.75 kN, respectively, to induce different levels of pore damage. The applied pressure was calculated as $P = F/A$, where F is the force applied on the piston. Thus, the applied peak stress, σ_{max}, was 2 MPa, 4 MPa, and 6 MPa accordingly. More details of the material preparation and the testing setup are given in the ESI.† Fig. 4(b) shows the stress–strain curves of dry pre-compression tests. The observed hysteresis behavior indicates that permanent mechanical deformation including the buckling and collapse of the nanopores occurred even at the peak stress, σ_{max}, as low as 2 MPa. With the increase of the peak stress, the associated loop area of hysteresis in the stress–strain curve increases, and the deformation of the nanopores becomes more severe as more nanopores are permanently deformed. Besides, due to the relatively wide pore size distribution in the silica gel (Fig. S9 in the ESI†), no clear elastic to plastic transition was observed in these dry pre-compression tests.

Pressure-induced liquid infiltration tests on LN systems were conducted on all the silica gel particles with or without dry pre-compression. Fig. 4(c–f) show the P–ΔV curves of various LN samples. Initially, the liquid did not enter the nanopores due to the surface hydrophobicity of the silica gel, and the porous particles may experience compression or/and bending deformation. As the external pressure reached a critical value, the capillary effect was overcome and the liquid was driven into the nanopores. Consequently, a stress plateau was observed, similar to the simulation results in Fig. 2 and 3.

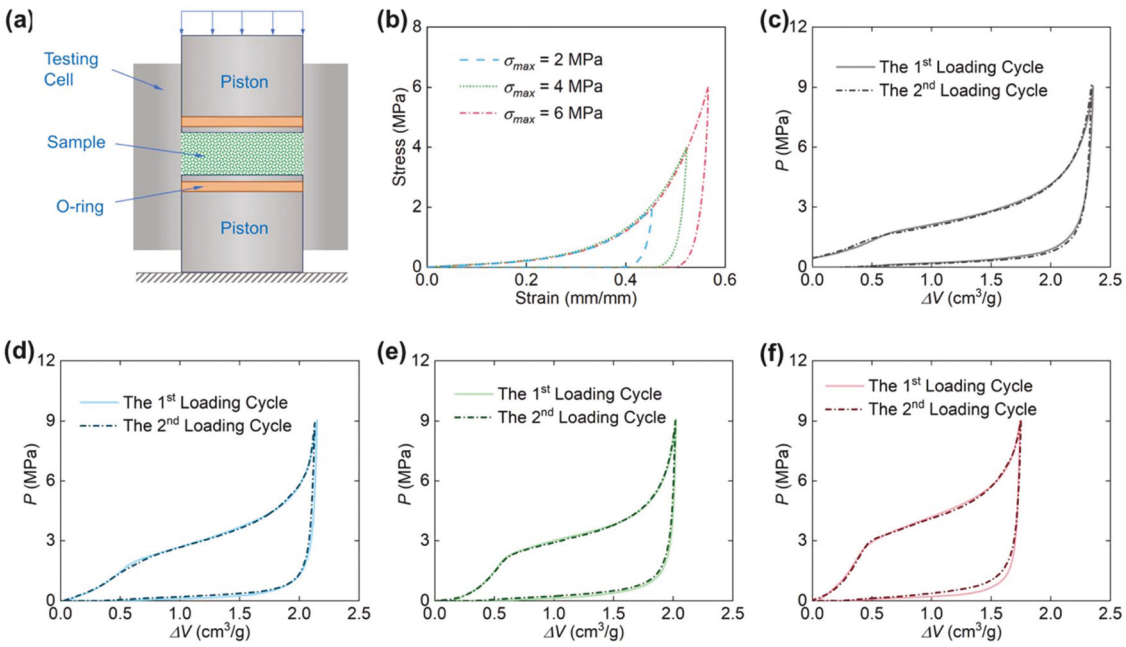

Fig. 4 Experiments of pressure-induced liquid infiltration on porous silica–lithium chloride (LiCl) aqueous solutions. (a) The schematic of the experimental setup. (b) Loading history of the dry pre-compression on empty silica gels under various peak stress σ_{max}. (c) Sorption isotherm curves of the LN system without dry pre-compression. (d) Sorption isotherm curves of the LN system with dry pre-compression at σ_{max} = 2 MPa. (e) Sorption isotherm curves of the LN system with dry pre-compression at σ_{max} = 4 MPa. (f) Sorption isotherm curves of the LN system with dry pre-compression at σ_{max} = 6 MPa. The loading rate for all experiments was 1 mm min^{-1}.

Once all the nanopores were filled, the system became incompressible. The width of the stress plateau reflected the specific nanopore volume of the silica gel specimens, ΔV_{sp}. The liquid infiltration pressure, P_{in}, is defined as the pressure at the midpoint of the stress plateau. For the LN system without pre-compression (*i.e.* σ_{max} = 0), P_{in} was about 2.6 MPa, high enough to deform nanopores in comparison with the dry pre-compression on particles, yet the liquid was successfully invaded, in agreement with the theoretical analysis and MD simulations, and ΔV_{sp} was around 1.60 $cm^3\ g^{-1}$. As the pre-compression peak stress σ_{max} increased from 0 to 6 MPa, P_{in} increased from 2.6 MPa to 4.2 MPa, and ΔV_{sp} of the corresponding LN decreased from 1.6 $cm^3\ g^{-1}$ to 1.10 $cm^3\ g^{-1}$. The results of all the liquid infiltration tests are summarized in Table 1. The increased P_{in} is in agreement with the liquid infiltration into small pores as the large pores collapsed prior to the dry pre-compression. The decreased ΔV_{sp} also agrees well with the increased collapse volume of nanoporous particles by the applied dry pre-compression shown in Fig. 4(b). P_{in} is smaller than that in simulations due to the larger pores used in the experiments.

To further confirm that the whole process was dominated by liquid infiltration rather than permanent mechanical deformation of nanopores under compression on LN systems, the nanoporous silica particles were collected by filtering out the liquid, and then thoroughly rinsed with ethanol and warm DI water to remove the residual electrolytes in the nanopores followed by drying in air (the details of the recycling process can be found in the ESI†). The recycled nanoporous silica particles were mixed with the same amount of saturated LiCl solution and tested under quasi-static compression. The P–ΔV curves are plotted as the second loading–unloading cycles in Fig. 4(c–f). The liquid infiltration performance of all silica gel samples with different levels of dry pre-compression remained the same, indicating that the nanoporous structures were not further deformed in the first loading–unloading cycle in the presence of the non-wettable liquid. Please note that the nanoporous silica particles have 3-D porous structures, as shown in Fig. S10.† When suspended in a liquid solution, upon compression, the liquid invades in a spatial dimension and no radial collapse deformation is expected.

In summary, we have investigated both liquid infiltration and cell wall buckling of a liquid nanofoam system under compression and presented a theoretical map for understanding the fundamental competition of these two deformation mechanisms. The molecular dynamics simulations were performed and the results show that the liquid suppresses the axial buckling deformation of the nanopores and invades into the nanopores. In contrast, when the radial collapse pressure of nanopores is smaller than the liquid infiltration pressure, the radial collapse deformation leads to the damage of the nanopore before the infiltration of the liquid, and thus, liquid infiltration is interrupted. These findings have been further confirmed by pressure-induced infiltration compression experiment on a silica-based LN system. The present study not only addresses the long-standing and puzzling question between liquid infiltration and nanopore buckling in the measurement of the properties of relevance to porous structures in a broad range of materials, but also provides quantitative guidance for designing a high-performance liquid nanofoam energy absorption system and nanofluidics-enabled devices.

Table 1 ΔV_{sp} and P_{in} of various LN samples

σ_{max} (MPa)	ΔV_{sp} ($cm^3\ g^{-1}$)	P_{in} (MPa)
0	1.60	2.6
2	1.45	3.2
4	1.30	3.4
6	1.10	4.2

Conflicts of interest

There are no conflicts to declare.

Acknowledgements

B. X. acknowledges the start-up funds at the University of Virginia and NSF-CBET-1805451 and W. L. acknowledges the start-up funds at Michigan State University and NSF-CBET-1803695.

References

1 R. Danielson and P. Sutherland, *Methods of Soil Analysis: Part 1—Physical and Mineralogical Methods*, 1986, pp. 443–461.
2 B. Xu, Y. Qiao and X. Chen, *J. Mech. Phys. Solids*, 2014, **62**, 194–208.
3 X. Chen, B. Xu and L. Liu, *Appl. Mech. Rev.*, 2014, **66**, 050803.
4 V. Eroshenko, R.-C. Regis, M. Soulard and J. Patarin, *J. Am. Chem. Soc.*, 2001, **123**, 8129–8130.
5 M. Z. Li and W. Y. Lu, *AIP Adv.*, 2017, **7**, 055312.
6 J. Zhao, P. J. Culligan, J. T. Germaine and X. Chen, *Langmuir*, 2009, **25**, 12687–12696.
7 B. Xu, X. Chen, W. Lu, C. Zhao and Y. Qiao, *Appl. Phys. Lett.*, 2014, **104**, 203107.
8 Y. Qiao, G. Cao and X. Chen, *J. Am. Chem. Soc.*, 2007, **129**, 2355–2359.
9 B. Xu, Y. Qiao, Q. Zhou and X. Chen, *Langmuir*, 2011, **27**, 6349–6357.
10 Y. Qiao, L. Liu and X. Chen, *Nano Lett.*, 2009, **9**, 984–988.
11 B. Xu, B. Wang, T. Park, Y. Qiao, Q. Zhou and X. Chen, *J. Chem. Phys.*, 2012, **136**, 184701.
12 W. H. Duan and Q. Wang, *ACS Nano*, 2010, **4**, 2338–2344.
13 J. Shim, C. Perdigou, E. R. Chen, K. Bertoldi and P. M. Reis, *Proc. Natl. Acad. Sci. U. S. A.*, 2012, **109**(16), 5978–5983.
14 J. Feliciano, C. Tang, Y. Zhang and C. Chen, *J. Appl. Phys.*, 2011, **109**, 084323.

15 Y. Zhang, C. Wang, W. Duan, Y. Xiang and Z. Zong, *Nanotechnology*, 2009, **20**, 395707.
16 P. Tangney, R. B. Capaz, C. D. Spataru, M. L. Cohen and S. G. Louie, *Nano Lett.*, 2005, **5**, 2268–2273.
17 D. Sun, D. Shu, M. Ji, F. Liu, M. Wang and X. Gong, *Phys. Rev. B: Condens. Matter Mater. Phys.*, 2004, **70**, 165417.
18 P. Mark and L. Nilsson, *J. Phys. Chem. A*, 2001, **105**, 9954–9960.
19 S. Munetoh, T. Motooka, K. Moriguchi and A. Shintani, *Comput. Mater. Sci.*, 2007, **39**, 334–339.
20 E. R. Cruz-Chu, A. Aksimentiev and K. Schulten, *J. Phys. Chem. B*, 2006, **110**, 21497–21508.
21 D. J. Evans and B. L. Holian, *J. Chem. Phys.*, 1985, **83**, 4069–4074.
22 S. Plimpton, *J. Comput. Phys.*, 1995, **117**, 1–19.
23 G. Hummer, J. C. Rasaiah and J. P. Noworyta, *Nature*, 2001, **414**, 188.

